JOURNAL OF COMPUTATIONAL PHYSICS **144,** 257–279 (1998)
ARTICLE NO. CP975803

A Massively Parallel Three-Dimensional Hybrid Code for Simulating Ion-Driven Parametric Instabilities

H. X. Vu

Applied Theoretical and Computational Division, Los Alamos National Laboratory, Los Alamos, New Mexico 87545

Received June 3, 1996; revised May 30, 1997

A massively parallel three-dimensional hybrid particle-in-cell (PIC) code, implemented on the CRAY-T3D, is presented. The code is based on a physical model described in a previous report where the electrons are modeled as an adiabatic fluid with an arbitrary ratio of specific heats γ and the electromagnetic field model is based on a temporal Wentzel–Krammers–Brillouin (WKB) approximation. On a CRAY-T3D with 512 processors, the code requires about $0.6\,\mu$s/particle/time step. The largest test problem performed with this code consists of a computational mesh of $4096 \times 64 \times 64$ (16 million) cells, a total of 256 million particles, and corresponds to a plasma volume of $50\,\mu\text{m} \times 20\,\mu\text{m} \times 20\,\mu\text{m}$ (approximately $150\,\lambda \times 60\,\lambda \times 60\,\lambda$, where λ is the laser's vacuum wavelength). We believe this code is the first PIC computational tool capable of simulating low-frequency ion-driven parametric instabilities in a large, three-dimensional plasma volume and offers a unique opportunity for examining issues that are potentially vital to inertial confinement fusion (ICF), e.g., nonlinear ion kinetic effects and their role in nonlinear saturation mechanisms in three dimensions. Test simulations of the self-focusing (SF) instability and of the self-focusing-induced deflection of a laser beam are presented.

Key Words: massively parallel; three-dimensional; particle-in-cell; parametric instabilities; laser-produced plasmas; stimulated Brillouin scattering.

1. INTRODUCTION

In inertial confinement fusion (ICF) applications an external high-frequency monochromatic electromagnetic wave such as a laser is employed to irradiate the plasma. The external monochromatic electromagnetic wave, due to its interaction with the plasma, can undergo either electron-driven or ion-driven parametric instabilities, and decays into various combinations of daughter waves [1]. Recent experiments [2–3] and fluid simulations [4–7] indicate that ion-driven parametric instabilities, which affect the propagation of external

0021-9991/98 $25.00

driving electromagnetic fields, are prevalent in current ICF plasmas of interest. Due to a multitude of spatial and temporal scales that exist in such plasmas and the fact that the external driving electromagnetic field is of high frequency, general-purpose explicit, implicit, and hybrid PIC algorithms [8–32] are either incapable of simulating the actual physics, or computationally inefficient. In a recent work [33], a special-purpose hybrid PIC model was presented in which the electrons are modeled as an adiabatic fluid with an arbitrary ratio of specific heats γ, and the electromagnetic field model is based on a temporal Wentzel–Krammers–Brillouin (WKB) approximation. This hybrid PIC model was implemented in two dimensions and was shown to model ion Landau damping, finite-Debye-length effects, aperiodically driven stimulated Brillouin scattering (SBS), and the interaction between SBS and the filamentation instability (FI) correctly [33].

In this paper, we present HERCULES, a massively parallel three-dimensional hybrid PIC code, implemented on the CRAY-T3D, appropriate for modeling low-frequency ion-driven parametric instabilities in three dimensions. This code is basically a parallelization and three dimensional extension of the earlier two-dimensional code [33]. The rest of this paper is divided into three sections. In Sections 2, we described the physical model appropriate for simulating ion-driven parametric instabilities. In Section 3, parallel algorithms for solving the electromagnetic and electrostatic field equations are presented. Timing studies regarding the performance and parallel efficiency of HERCULES are presented in Section 4. In Section 5, test simulations of the self-focusing (SF) instability and of the self-focusing-induced deflection of a laser beam are presented. Section 6 is a summary of our results and conclusions based on these results.

2. PHYSICAL MODEL

In the presence of an electromagnetic pump wave of frequency ω_0, the vector potential $\mathbf{A}(\mathbf{x}, t)$ within the plasma can be written as

$$\mathbf{A}(\mathbf{x}, t) = \tfrac{1}{2}(\mathbf{a}(\mathbf{x}, t)\mathbf{e}^{-i\omega_0 t} + \mathbf{a}^*(\mathbf{x}, t)\mathbf{e}^{i\omega_0 t}), \tag{1}$$

where $\mathbf{a}(\mathbf{x}, t)$ is complex-valued. The temporal field envelope $\mathbf{a}$ is assumed to vary on a time scale much longer than $2\pi/\omega_0$. The hybrid model employed in this paper treats the electrons as an adiabatic fluid with an arbitrary ratio of specific heats γ. The ions are treated as finite-size particles, allowing ion kinetic effects to be modeled correctly. Because $k\lambda_{\mathrm{De}} \sim O(1)$ (λ_{De} is the electron Debye length) for current ICF plasmas of interest, it is necessary for Poisson equation to be included in the model, and the plasma is not taken to be locally quasineutral. The electromagnetic field is analyzed using the temporal WKB approximation described by Eq. (1), resulting in a nonlinear Schrodinger equation for the temporal field envelope. A detailed derivation of our hybrid model can be found elsewhere [33]. The hybrid model can be summarized as

$$\left.\begin{aligned} & i\left(\frac{2\omega_0}{c^2}\right)\frac{\partial \mathbf{a}}{\partial t} + \nabla^2\mathbf{a} + \mathrm{K}^2\mathbf{a} = 0 \\ & \mathrm{K}^2 \equiv \frac{1}{c^2}\left[\omega_0^2 - \left(\omega_p^2 + \Omega_p^2\right)\right] \\ & \omega_p^2 \equiv \frac{4\pi e^2 n_e}{m_e} \\ & \Omega_p^2 \equiv \sum_i \frac{4\pi e^2 Z_i^2 n_i}{m_i} \end{aligned}\right\} \tag{2}$$

$$e\phi - \frac{e^2}{4m_e c^2}\mathbf{a}\cdot\mathbf{a}^* - f(\gamma, n_e) = \alpha \tag{3}$$

$$f(\gamma, n_e) = \begin{cases} T_{e0}\ln\left(\dfrac{n_e}{n_{e0}}\right) & \text{if } \gamma = 1 \\ T_{e0}\left(\dfrac{\gamma}{\gamma-1}\right)\left(\dfrac{n_e}{n_{e0}}\right)^{\gamma-1} & \text{if } \gamma \neq 1 \end{cases}$$

$$\int \boldsymbol{\nabla}\phi \cdot d\boldsymbol{\sigma} = 0 \tag{4}$$

$$\nabla^2\phi = 4\pi e\left(n_e - \sum_i Z_i n_i\right) \tag{5}$$

$$\left.\begin{aligned} m_i\frac{d\mathbf{u}_{i\mathrm{L}}}{dt} &= -eZ_i\boldsymbol{\nabla}\phi - \frac{e^2Z_i^2}{4m_i c^2}\boldsymbol{\nabla}(\mathbf{a}\cdot\mathbf{a}^*) \\ \frac{d\mathbf{x}_i}{dt} &= \mathbf{u}_{i\mathrm{L}} \end{aligned}\right\}. \tag{6}$$

Here, c is the speed of light, m_e and m_i are the electron and ion masses, Z_i is the ionization state of the ith ion species, n_e and n_i are the electron and ion number densities, γ is the electron ratio of specific heats, T_{e0} is the initial electron temperature, and $d\boldsymbol{\sigma}$ is a surface area element. Each finite-size particle ion carries a longitudinal velocity $\mathbf{u}_{i\mathrm{L}}$ and position $\mathbf{x}_i$. Equations (2)–(6) constitute our hybrid model and are solved in three-dimensional Cartesian space to model ion-driven parametric instabilities.

It is noted here that in deriving the nonlinear Schrodinger equation, Eqs. (2), the transverse plasma current response is assumed to be $\mathbf{J}_T \approx -(1/4\pi c^2)(\omega_p^2 + \Omega_p^2)\mathbf{A}$ [33]. For sufficiently low-density plasmas, as is the case with the current ICF regime of interest, this is a good approximation. Henceforth, one shall always operate at sufficiently low densities that Eqs. (2) are valid.

For situations in which the plasma density is sufficiently high, the transverse plasma response must be written as

$$\mathbf{J}_T = -\frac{1}{4\pi c^2}\left(\omega_p^2 + \Omega_p^2\right)\mathbf{A} - \boldsymbol{\nabla}\chi$$
$$\nabla^2\chi \equiv -\frac{1}{4\pi c^2}\mathbf{A}\cdot\boldsymbol{\nabla}\left(\omega_p^2 + \Omega_p^2\right),$$

and the nonlinear Schrodinger equation, Eqs. (2), must be modified accordingly. Such a general formulation, together with electron kinetic effects, are not within the scope of this paper and are the subject of ongoing research.

3. NUMERICAL ALGORITHM

Each ion particle carries a charge q_p, position $\mathbf{x}_p$, and velocity $\mathrm{u}_{p\mathrm{L}}$. Associated with each particle is an interpolation function $S(\mathbf{x} - \mathbf{x}_p)$ that determines how the particle charges are interpolated onto the computational mesh. In our three-dimensional Cartesian implementation of Eqs. (2)–(6), $S(\mathbf{x})$ is chosen to be a tri-quadratic B-spline [9], and the ion density

is interpolated onto the computational mesh as

$$eZ_i n_i(\mathbf{x}, t) = \sum_{p\in i} q_p S(\mathbf{x}(t) - \mathbf{x}_p).$$

A. *Temporal Discretization*

Because the temporal discretization scheme for Eqs. (2)–(6) employed in this paper is identical to that presented and analyzed in an earlier paper [33], we will discuss only the salient features and properties of the scheme. The interested reader can find more complete discussions and analyses of the scheme elsewhere [33]. The nonlinear Schrodinger equation, Eq. (2), is advanced in time using the Crank–Nicolson algorithm. The ion equations of motion, Eqs. (6), are advanced using the standard leapfrog algorithm in which the velocity and position are advanced in time alternatively. It was shown that the combined Crank–Nicolson/leapfrog algorithm conserves the laser energy rigorously and is numerically stable for $\Omega_p \delta t < 1$ [33].

Using the Crank–Nicolson method [33], the electromagnetic field equation, Eq. (2), is advanced in time as

$$\left.\begin{aligned} i\left(\frac{2\omega_0}{c^2}\right)\frac{\mathbf{a}^{(\mathrm{n})} - \mathbf{a}^{(\mathrm{n}-1)}}{\delta t} + \frac{1}{2}\nabla^2\left(\mathbf{a}^{(\mathrm{n})} + \mathbf{a}^{(\mathrm{n}-1)}\right) \\ + \frac{1}{4}\left(\left[\mathrm{K}^{(\mathrm{n})}\right]^2 + \left[\mathrm{K}^{(\mathrm{n}-1)}\right]^2\right)\left(\mathbf{a}^{(\mathrm{n})} + \mathbf{a}^{(\mathrm{n}-1)}\right) \end{aligned}\right\} = 0, \tag{7}$$

where

$$\left[\mathrm{K}^{(\mathrm{n})}\right]^2 = \omega_0^2 - \left[\omega_p^{(\mathrm{n})}\right]^2 - \left[\Omega_p^{(\mathrm{n})}\right]^2, \quad \left[\mathrm{K}^{(\mathrm{n}-1)}\right]^2 = \omega_0^2 - \left[\omega_p^{(\mathrm{n}-1)}\right]^2 - \left[\Omega_p^{(\mathrm{n}-1)}\right]^2$$

$$\left[\omega_p^{(\mathrm{n})}\right]^2 = \frac{4\pi e^2 n_e^{(\mathrm{n})}}{m_e}, \qquad \left[\omega_p^{(\mathrm{n}-1)}\right]^2 = \frac{4\pi e^2 n_e^{(\mathrm{n}-1)}}{m_e}$$

$$\left[\Omega_p^{(\mathrm{n})}\right]^2 = \sum_i \frac{4\pi e^2 Z_i^2 n_i^{(\mathrm{n})}}{m_i}, \qquad \left[\Omega_p^{(\mathrm{n}-1)}\right]^2 = \sum_i \frac{4\pi e^2 Z_i^2 n_i^{(\mathrm{n}-1)}}{m_i}$$

$$eZ_i n_i^{(\mathrm{n})} = \sum_{p\in i} q_p S\left(\mathbf{x} - \mathbf{x}_p^{(\mathrm{n})}\right), \qquad eZ_i n_i^{(\mathrm{n}-1)} = \sum_{p\in i} q_p S\left(\mathbf{x} - \mathbf{x}_p^{(\mathrm{n}-1)}\right).$$

The superscripts $(\mathrm{n}-\frac{1}{2})$, (n), $(\mathrm{n}+\frac{1}{2})$, and $(\mathrm{n}+1)$ refer to the time levels $t_\mathrm{n} - \delta t/2$, t_n, $t_\mathrm{n} + \delta t/2$, and $t_{\mathrm{n}+1}$, where $t_\mathrm{n} \equiv \mathrm{n}\delta t$.

The electrostatic field equations, Eqs. (3)–(5), are simply evaluated at the time level n [33]:

$$\left.\begin{aligned} e\phi^{(\mathrm{n})} - \frac{e^2}{4m_e c^2}\mathbf{a}^{(\mathrm{n})}\cdot\mathbf{a}^{*(\mathrm{n})} - f\left(\gamma, n_e^{(\mathrm{n})}\right) = \alpha^{(\mathrm{n})} \\ \nabla^2\phi^{(\mathrm{n})} = 4\pi e\left(n_e^{(\mathrm{n})} - \sum_i Z_i n_i^{(\mathrm{n})}\right) \end{aligned}\right\} \tag{8}$$

$$\int \nabla\phi^{(\mathrm{n})}\cdot d\boldsymbol{\sigma} = 0. \tag{9}$$

Using the leapfrog algorithm in which the pair of variables $\mathbf{x}$ and $\mathbf{u}_{p\mathrm{L}}$ are advanced in time alternately [33], the ion equations of motion, Eqs. (6), are approximated as

$$\begin{aligned}\frac{\mathbf{u}_{p\mathrm{L}}^{(\mathrm{n}+1/2)}-\mathbf{u}_{p\mathrm{L}}^{(\mathrm{n}-1/2)}}{\delta t} &= -\frac{eZ_i}{m_i}\boldsymbol{\nabla}\phi^{(\mathrm{n})}-\left(\frac{eZ_i}{2m_ic}\right)^2\boldsymbol{\nabla}\left(\mathbf{a}^{(\mathrm{n})}\cdot\mathbf{a}^{*(\mathrm{n})}\right)\\ \frac{\mathbf{x}_p^{(\mathrm{n}+1)}-\mathbf{x}_p^{(\mathrm{n})}}{\delta t} &= \mathbf{u}_{p\mathrm{L}}^{(\mathrm{n}+1/2)}.\end{aligned} \tag{10}$$

At time $t=t_{\mathrm{n}-1}$, when the field quantities $\mathbf{a}^{(\mathrm{n}-1)}$ and $\phi^{(\mathrm{n}-1)}$, electron density $n_e^{(\mathrm{n}-1)}$, particle velocities $\mathbf{u}_{p\mathrm{L}}^{(\mathrm{n}-1/2)}$ and positions $\mathbf{x}_p^{(\mathrm{n})}$ are known, Eqs. (7)–(9) are solved for $\mathbf{a}^{(\mathrm{n})}$, $\phi^{(\mathrm{n})}$, $n_e^{(\mathrm{n})}$, and $\alpha^{(\mathrm{n})}$. Equations (10) are then advanced in order to obtain the time-advanced velocities $\mathbf{u}_{p\mathrm{L}}^{(\mathrm{n}+1/2)}$ and positions $\mathbf{x}_p^{(\mathrm{n}+1)}$.

B. *Spatial Discretization*

In this section, Eqs. (7)–(10), the time-discrete representation of our hybrid model, are implemented in Cartesian three-dimensional space. This is an obvious extension of an earlier Cartesian two-dimensional code [33].

Consider a computational domain consisting of a rectangular box with $0\le x\le L_x$, $0\le y\le L_y$, and $0\le z\le L_z$. The computational mesh is staggered and consists of $(\mathrm{N}_x-1)\times(\mathrm{N}_y-1)\times(\mathrm{N}_z-1)$ rectangular cells of equal size. $\mathbf{x}_{klm}^v$, the physical coordinate of the vertices of the computation cells, and $\mathbf{x}_{klm}^c$, the physical coordinate of the centers of the computational cells, are specified as

$$\begin{aligned}\mathbf{x}_{klm}^v &= (k-1)\delta x\hat{\mathbf{e}}_x+(l-1)\delta y\hat{\mathbf{e}}_y+(m-1)\delta z\hat{\mathbf{e}}_z\\ \mathbf{x}_{klm}^c &= \mathbf{x}_{klm}^v+\frac{\delta x}{2}\hat{\mathbf{e}}_x+\frac{\delta y}{2}\hat{\mathbf{e}}_y+\frac{\delta z}{2}\hat{\mathbf{e}}_z,\end{aligned}$$

where $\delta x\equiv \mathrm{L}_x/(\mathrm{N}_x-1)$, $\delta y\equiv \mathrm{L}_y/(\mathrm{N}_y-1)$, and $\delta z\equiv \mathrm{L}_z/(\mathrm{N}_z-1)$. Here, k, l, and m are indices labeling the computational cells.

The electron density n_e, ion density n_i, electrostatic potential ϕ, and the pump electromagnetic field $\mathbf{a}$ are cell-centered quantities. The ion density $n_i^{(\mathrm{n})}$ is interpolated from known particle data onto the cell centers as

$$n_{i,klm}^{(\mathrm{n})}=\sum_{p\in i}q_pS\left(\mathbf{x}_{klm}^c-\mathbf{x}_p^{(\mathrm{n})}\right), \tag{11}$$

where, as previously mentioned, $S(\mathbf{x}_{klm}^c-\mathbf{x})$ is a tri-quadratic B-spline [9]. The spatially discrete representation of Eqs. (7)–(9) are [33]

$$\left.\begin{aligned}i\left(\frac{2\omega_0}{c^2}\right)\frac{\mathbf{a}_{klm}^{(\mathrm{n})}-\mathbf{a}_{klm}^{(\mathrm{n}-1)}}{\delta t}+\frac{1}{2}\left(D_{klm}\left[\mathbf{a}^{(\mathrm{n})}\right]+D_{klm}\left[\mathbf{a}^{(\mathrm{n}-1)}\right]\right)\\ +\frac{1}{4}\left(\left[\mathrm{K}_{klm}^{(\mathrm{n})}\right]^2+\left[\mathrm{K}_{klm}^{(\mathrm{n}-1)}\right]^2\right)\left(\mathbf{a}_{klm}^{(\mathrm{n})}+\mathbf{a}_{klm}^{(\mathrm{n}-1)}\right)\end{aligned}\right\}=0 \tag{12}$$

$$\begin{aligned}e\phi_{klm}^{(\mathrm{n})}-\frac{e^2}{4m_ec^2}\mathbf{a}_{klm}^{(\mathrm{n})}\cdot\mathbf{a}_{klm}^{*(\mathrm{n})}-f\left(\gamma,n_{e,klm}^{(\mathrm{n})}\right)&=\alpha^{(\mathrm{n})}\\ D_{klm}\left[\phi^{(\mathrm{n})}\right]&=4\pi e\left(n_{e,klm}^{(\mathrm{n})}-\sum_i Z_in_{i,klm}^{(\mathrm{n})}\right)\end{aligned} \tag{13}$$

$$\left.\begin{aligned}
&\delta x\,\delta z\sum_{k=1}^{\mathrm{N}_x-1}\left(\frac{\phi^{(\mathrm{n})}_{k\mathrm{N}_y m}-\phi^{(\mathrm{n})}_{k\mathrm{N}_y-1m}}{\delta y}-\frac{\phi^{(\mathrm{n})}_{k1m}-\phi^{(\mathrm{n})}_{k0m}}{\delta y}\right)\\
&+\delta y\,\delta z\sum_{l=1}^{\mathrm{N}_y-1}\left(\frac{\phi^{(\mathrm{n})}_{\mathrm{N}_x lm}-\phi^{(\mathrm{n})}_{\mathrm{N}_x-1lm}}{\delta x}-\frac{\phi^{(\mathrm{n})}_{1lm}-\phi^{(\mathrm{n})}_{0lm}}{\delta x}\right)\\
&+\delta x\,\delta y\sum_{m=1}^{\mathrm{N}_z-1}\left(\frac{\phi^{(\mathrm{n})}_{kl\mathrm{N}_z}-\phi^{(\mathrm{n})}_{kl\mathrm{N}_z-1}}{\delta z}-\frac{\phi^{(\mathrm{n})}_{kl1}-\phi^{(\mathrm{n})}_{kl0}}{\delta z}\right)
\end{aligned}\right\}=0, \tag{14}$$

where the numerical Laplacian operator is defined as follows: It should be noted here that $\phi^{(\mathrm{n})}_{0lm}$, $\phi^{(\mathrm{n})}_{\mathrm{N}_x lm}$, $\phi^{(\mathrm{n})}_{k0m}$, $\phi^{(\mathrm{n})}_{k\mathrm{N}_y m}$, $\phi^{(\mathrm{n})}_{kl0}$, and $\phi^{(\mathrm{n})}_{kl\mathrm{N}_z}$, refer to values of $\phi^{(\mathrm{n})}$ in the ghost cells.

At time $t=t_{\mathrm{n}-1}$, when $n_e^{(\mathrm{n}-1)}$, $\phi^{(\mathrm{n}-1)}$, and $\mathbf{a}^{(\mathrm{n}-1)}$ are known, the nonlinearly coupled Eqs. (12)–(14) must be solved in order to obtain $n_e^{(\mathrm{n})}$, $\phi^{(\mathrm{n})}$, and $\mathbf{a}^{(\mathrm{n})}$. The ion particles are advanced in time using a spatially discrete representation of Eqs. (10),

$$\begin{aligned}
\frac{\mathbf{u}_{p\mathrm{L}}^{(\mathrm{n}+1/2)}-\mathbf{u}_{p\mathrm{L}}^{(\mathrm{n}-1/2)}}{\delta t}&=-\frac{eZ_i}{m_i}\tilde{\mathbf{E}}_p^{(\mathrm{n})}\\
\frac{\mathbf{x}_p^{(\mathrm{n}+1)}-\mathbf{x}_p^{(\mathrm{n})}}{\delta t}&=\mathbf{u}_{p\mathrm{L}}^{(\mathrm{n}+1/2)},
\end{aligned} \tag{15}$$

where the effective electric field acting on each particle, $\tilde{\mathbf{E}}_p^{(\mathrm{n})}$, is interpolated from the cell vertices to the known particle positions $\mathbf{x}_p^{(\mathrm{n})}$ by means of a tri-linear B-spline [9].

The effective electric field at the cell vertices is defined as

$$\begin{aligned}
\tilde{\mathbf{E}}^{(\mathrm{n})}_{i,klm}\equiv\frac{1}{4}&\left(\frac{\Phi^{(\mathrm{n})}_{i,klm}-\Phi^{(\mathrm{n})}_{i,k-1lm}}{\delta x}+\frac{\Phi^{(\mathrm{n})}_{i,kl-1m}-\Phi^{(\mathrm{n})}_{i,k-1l-1m}}{\delta x}\right.\\
&\left.+\frac{\Phi^{(\mathrm{n})}_{i,klm-1}-\Phi^{(\mathrm{n})}_{i,k-1lm-1}}{\delta x}+\frac{\Phi^{(\mathrm{n})}_{i,kl-1m-1}-\Phi^{(\mathrm{n})}_{i,k-1l-1m-1}}{\delta x}\right)\hat{\mathbf{e}}_x\\
+\frac{1}{4}&\left(\frac{\Phi^{(\mathrm{n})}_{i,klm}-\Phi^{(\mathrm{n})}_{i,kl-1m}}{\delta y}+\frac{\Phi^{(\mathrm{n})}_{i,k-1lm}-\Phi^{(\mathrm{n})}_{i,k-1l-1m}}{\delta y}\right.\\
&\left.+\frac{\Phi^{(\mathrm{n})}_{i,klm-1}-\Phi^{(\mathrm{n})}_{i,kl-1m-1}}{\delta y}+\frac{\Phi^{(\mathrm{n})}_{i,k-1lm-1}-\Phi^{(\mathrm{n})}_{i,k-1l-1m-1}}{\delta y}\right)\hat{\mathbf{e}}_y\\
+\frac{1}{4}&\left(\frac{\Phi^{(\mathrm{n})}_{i,klm}-\Phi^{(\mathrm{n})}_{i,klm-1}}{\delta z}+\frac{\Phi^{(\mathrm{n})}_{i,k-1lm}-\Phi^{(\mathrm{n})}_{i,k-1lm-1}}{\delta z}\right.\\
&\left.+\frac{\Phi^{(\mathrm{n})}_{i,kl-1m}-\Phi^{(\mathrm{n})}_{i,kl-1m-1}}{\delta z}+\frac{\Phi^{(\mathrm{n})}_{i,k-1l-1m}-\Phi^{(\mathrm{n})}_{i,k-1l-1m-1}}{\delta z}\right)\hat{\mathbf{e}}_z
\end{aligned}$$

$$\Phi_i^{(\mathrm{n})}\equiv\phi^{(\mathrm{n})}+\frac{eZ_i}{4m_i c^2}\mathbf{a}^{(\mathrm{n})}\cdot\mathbf{a}^{*(\mathrm{n})}.$$

Here, i denotes the ion species to which the particle p belongs.

C. *Parallel Decomposition of Computational Domain*

The laser is taken to propagate primarily in the x direction, and this choice necessitates the use of many more computation cells in the x direction than in the y and z directions.

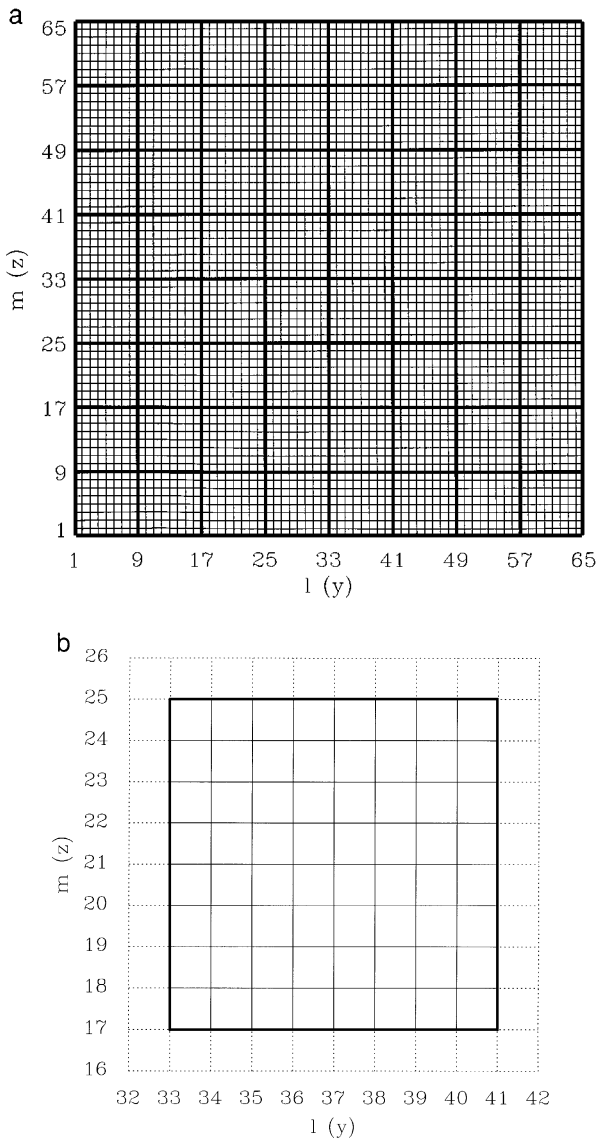

FIG. 1. The two-dimensional decomposition of the three-dimensional computational volume is illustrated. No decomposition is performed in the x (k) direction. As a specific example, the computational mesh consists of 64×64 cells in the y–z (l–m) plane and 64 processors are used. The thin solid lines denote the boundaries between adjacent computational cells, and the thick solid lines denote the boundaries between the processors' private computational volumes. Each processor carries a single layer of ghost cells immediately surrounding its private computational volume, as illustrated by the dotted lines.

A two-dimensional parallel decomposition in the y–z plane has been applied to the three-dimensional computational mesh, as illustrated in Figs. 1, where, as a specific example, the computational mesh consists of 64×64 cells in the y–z (l–m) plane and 64 processors are used. The computational volume is partitioned into N_{pro} equal subdomains, where N_{pro} is the number of processors, and each subdomain is assigned to a processor and is henceforth referred to as that processor's private computational volume. In Figs. 1, the thin solid lines denote the boundaries between adjacent computational cells, and the thick solid lines

denote the boundaries between the processors' private computational volumes. No parallel decomposition is performed in the x direction, and each processor holds field data and interpolated density data on cell centers interior to the processor's private computational volume. In addition, each processor also carries a single layer of ghost cells immediately surrounding its private computational volume, as illustrated by the dotted lines in Fig. 1b.

The particles are initially loaded into the processors and are subsequently reassigned among the processors (through the use of interprocessor communications) as the particles' positions evolve, in such a manner which ensures that each particle's position is interior to the private computational volume of the processor to which it is assigned.

D. *Parallel Algorithm for Solving Field Equations*

The nonlinearly coupled field equations, Eqs. (12)–(14), can be solved by means of a splitting algorithm where the equations are first linearized, and the resulting linearized equations are then solved within a triple-nested modified Newton–Raphson iteration which, upon convergence, yields solutions to the original nonlinearly coupled equations, Eqs. (12)–(14). A detailed description of the method can be found in an earlier paper [33]. In the present work, Eqs. (12)–(14) are solved exactly as outlined in [33]. However, the present work differs from [33] in that each linearized equation is solved by means of a parallel algorithm in three dimensions, to be discussed below. Numerical analyses of the properties of the parallel algorithms, wherever appropriate, shall also be presented.

Following Ref. [33], the nonlinear Schrodinger equation, Eq. (12), is linearized about $\mathbf{a}_{\mathrm{NR}}^{(\mathrm{n})}$ and $[\mathrm{K}_{\mathrm{NR}}^{(\mathrm{n})}]^2$, Newton–Raphson iterative approximations of $\mathbf{a}^{(\mathrm{n})}$ and $[\mathrm{K}^{(\mathrm{n})}]^2$ (cf. Eqs. (24) of Ref. [33]), and the resulting equation can be written in the canonical block-matrix form

$$\mathrm{C}_{lm}\mathbf{w}_{lm} + \mathrm{N}_{lm}(\mathbf{w}_{l+1,m} + \mathbf{w}_{l-1,m}) + \mathrm{E}_{lm}(\mathbf{w}_{l,m+1} + \mathbf{w}_{l,m-1}) = \mathbf{b}_{lm} \tag{16}$$

with $1 \le l \le \mathrm{N}_y - 1$, $1 \le m \le \mathrm{N}_z - 1$; $\mathbf{w}_{lm}$ represents the Newton–Raphson correction for the electromagnetic field envelope on the computational line (l, m). The submatrices C_{lm}, N_{lm}, and E_{lm} are $\mathrm{N}_x \times \mathrm{N}_x$ sparse square matrices and are defined as

$$\mathrm{C}_{lm}^{k,k} = -\left(\frac{1}{\delta x^2} + \frac{1}{\delta y^2} + \frac{1}{\delta z^2}\right) + i\left(\frac{2\omega_0}{c^2\delta t}\right) + \frac{1}{4}\left(\left[\mathrm{K}_{klm}^{(\mathrm{n}-1)}\right]^2 + \left[\mathrm{K}_{\mathrm{NR},klm}^{(\mathrm{n})}\right]^2\right) + \frac{1}{2}\left[\frac{\partial\left[\mathrm{K}_{\mathrm{NR},klm}^{(\mathrm{n})}\right]^2}{\partial \mathbf{a}_{\mathrm{NR},klm}^{(\mathrm{n})}} \cdot \mathbf{a}_{\mathrm{NR},klm}^{(\mathrm{n})}\right]$$

$$\mathrm{C}_{lm}^{k,k\pm1} = \frac{1}{2\delta x^2}$$

$$\mathrm{N}_{lm}^{k,k} = \frac{1}{2\delta y^2}$$

$$\mathrm{E}_{lm}^{k,k} = \frac{1}{2\delta z^2},$$

where $1 \le k \le \mathrm{N}_x - 1$. All matrix elements not explicitly defined above are zero, i.e., C_{lm} is tridiagonal and N_{lm} and E_{lm} are diagonal. Note that the electromagnetic field envelope has been implicitly assumed to be linearly polarized. Although Eq. (16) can be modified slightly to accommodate different types of polarization, such tasks will be left to the interested reader.

Equation (16) is solved iteratively by means of the line–Jacobi method,

$$C_{lm}\mathbf{w}_{lm}^{M+1} = -N_{lm}\left(\mathbf{w}_{l+1,m}^{M} + \mathbf{w}_{l-1,m}^{M}\right) - E_{lm}\left(\mathbf{w}_{l,m+1}^{M} + \mathbf{w}_{l,m-1}^{M}\right) + \mathbf{b}_{lm}, \qquad (17)$$

with $1 \le l \le N_y - 1$ and $1 \le m \le N_z - 1$. Equation (17) can be solved by a standard tridiagonal solver simultaneously for all values of l and m. Interprocessor communications are required at the beginning of each line–Jacobi iteration because the ghost cells have to be reinitialized with the values of the electromagnetic field envelope resulting from the previous iteration. It is noted here that because the tridiagonal matrix equations described by Eq. (17) have time-dependent variable coefficients, they cannot be solved by cyclic reduction methods and are, therefore, not parallelizable. Consequently, the two-dimensional spatial decomposition described in Section 3C is most efficient because the x direction is inherently nonparallelizable for the particular line–Jacobi algorithm under consideration.

In general, the properties of the line–Jacobi iterative algorithm described by Eq. (17) cannot be determined because the matrix coefficients are functions of the indices k, l, and m. However, under simplified conditions (uniform electron and ion densities, and a sufficiently weak external electromagnetic field), an analysis can be performed to determine the stability and asymptotic convergence rate of the algorithm. Such an analysis is complicated and disruptive to the readability of the paper, and therefore has been deferred to the Appendix.

Under the aforementioned simplified conditions, it has been shown in the Appendix that the line–Jacobi iteration algorithm described by Eq. (17) is convergent if

$$\max\left\{ \frac{\left[\frac{1}{\delta y^2}\cos\left(\frac{\pi}{N_y}\right) + \frac{1}{\delta z^2}\cos\left(\frac{\pi}{N_z}\right)\right]^2}{\left[\frac{1}{\delta x^2} + \frac{1}{\delta y^2} + \frac{1}{\delta z^2} - \frac{1}{2}k_0^2 \pm \frac{1}{\delta x^2}\cos\left(\frac{\pi}{N_x}\right)\right]^2 + \left(\frac{2\omega_0}{c^2\delta t}\right)^2} \right\} < 1, \qquad (18)$$

where $k_0^2 \approx [K_{NR}^{(n)}]^2 \approx [K^{(n-1)}]^2$. Equation (18) places a contraint on δt, in addition to $\Omega_p \delta t < 1$, to ensure numerical stability of the hybrid algorithm. However, for most simulations of interest, these two constraints on δt are comparable, and the line–Jacobi algorithm for solving the Schrodinger equation does not reduce the overall simulation time step.

The Poisson equation, Eqs. (13)–(14), can be linearized (cf. Eqs. (26)–(28) of Ref. [33]), and the resulting equation is solved by the standard conjugate gradient algorithm (CGA) without preconditioning. The CGA scheme is particularly suitable for our lineadrized Poisson equation because the matrix equation can be shown to be symmetric positive-definite. The CGA scheme without preconditioning involves computing: (a) the numerical Laplacian D_{klm} operating on mesh arrays, and (b) inner products and sums of mesh arrays, e.g., computing $q_{klm} = r_{klm} + s_{klm}$ and $\beta = \sum_{klm} r_{klm} s_{klm}$, where q_{klm}, r_{klm}, and s_{klm} are mesh arrays.

The numerical Laplacian D_{klm} operated on the mesh array r_{klm},

$$D_{klm}[\mathbf{r}] \equiv \frac{r_{k+1lm} - 2r_{klm} + r_{k-1lm}}{(\delta x)^2} + \frac{r_{kl+1m} - 2r_{klm} + r_{kl-1m}}{(\delta y)^2} + \frac{r_{klm+1} - 2r_{klm} + r_{klm-1}}{(\delta z)^2},$$

is computed concurrently on all processors. Of course, prior to this step, interprocessor communications are performed to ensure that the ghost cells contain the necessary information on $\mathbf{r}$.

The vector addition $q_{klm} = r_{klm} + s_{klm}$ is a local operator and is performed concurrently on all processors. The inner product $\beta = \sum_{klm} r_{klm} s_{klm}$ is computed in two steps. First, each

processor is allowed to perform the inner product in its private computational volume. This step does not involve any communication among the processors and is therefore performed in parallel. Second, after each processor completes its task, the resulting data are communicated to a single master processor. The master processor subsequently performs the final summation of all available data to obtain the inner product β.

It should be mentioned here that because the initial ion densities are spatially uniform in the simulations, the particles are scattered evenly across the processors at $t = 0$. For simulations in which the external electromagnetic field is moderate or weak, the ion density perturbations are small ($|\delta n_i / n_i| \ll 1$). As a result, the particle ions do not tend to be spatially bunched, and load balance is well maintained throughout the simulation.

E. *Angular Resolution*

In simulations of stimulated scattering processes, the angular distribution (with respect to the incident laser) of scattered light is important. Thus, one needs to have an estimate of the maximum angular resolution. Such an estimate can be derived by noticing that the electromagnetic wave, described by Eq. (2), must have a wave number k_0:

$$k_0^2 = \frac{1}{c^2}(\omega_0^2 - \omega_p^2 - \Omega_p^2).$$

The largest wave number that can be resolved in the transverse plane (y–z plane) is given by

$$k_{\perp\max} = \left[\left(\frac{\pi}{\delta y}\right)^2 + \left(\frac{\pi}{\delta z}\right)^2\right]^{1/2}.$$

The largest scattering angle that can be resolved can then be written as

$$\theta_{\max} = \sin^{-1}\left[\min\left(1, \frac{k_{\perp\max}}{k_0}\right)\right].$$

For the simulations to be presented, where $\delta y = \delta z = \Delta$, $\theta_{\max}$ can be reduced to the form

$$\theta_{\max} \approx \sin^{-1}\left[\min\left(1, \frac{\lambda}{\Delta}\left[2\left(1 - \frac{n_e}{n_c}\right)\right]^{-1/2}\right)\right],$$

where λ is the laser's vacuum wavelength.

F. *Boundary and Initial Conditions*

The simulations to be presented in Section 4 are periodic in the y and z directions, and aperiodic in the x direction. The laser, to be Gaussian and diffraction-limited with a specified f-number, enters and simulation domain at $x = 0$, and leaves the simulation domain at $x = \mathrm{L}_x$. The corresponding boundary conditions for the scalar and vector potentials are

$$\begin{aligned}
\phi(0, y, z, t) &= 0 \\
\hat{\mathbf{e}}_x \cdot \boldsymbol{\nabla}\phi(\mathrm{L}_x, y, z, t) &= 0 \\
\hat{\mathbf{e}}_x \cdot \boldsymbol{\nabla}\mathbf{a}(0, y, z, t) &= i\mathrm{K}(0, y, z, t)(2\mathbf{a}_0(y, z) - \mathbf{a}(0, y, z, t)) \\
\hat{\mathbf{e}}_x \cdot \boldsymbol{\nabla}\mathbf{a}(\mathrm{L}_x, y, z, t) &= i\mathrm{K}(\mathrm{L}_x, y, z, t)\,\mathbf{a}(\mathrm{L}_x, y, z, t).
\end{aligned}$$

Here, $\mathbf{a}_0(y, z)$ is a specified function and corresponds to the incident electromagnetic wave at $x = 0$. $\mathbf{a}_0$ is related to the incident laser intensity I as

$$\mathbf{a}_0(y, z) \cdot \mathbf{a}_0^*(y, z) = \left(\frac{8\pi}{c\omega_0^2}\right) \mathrm{I}(y, z).$$

For the simulations under consideration in which the laser is taken to be a diffraction-limited Gaussian beam $\mathbf{a}_0$ is specified as

$$\mathbf{a}_0(y, z) = \hat{\mathbf{e}}_z \frac{\sigma_{y0}\sigma_{z0}}{\sigma_y(0)\,\sigma_z(0)} \left(\frac{8\pi \mathrm{I}_0}{c\omega_0^2}\right)^{1/2} \exp\left[-\frac{1}{4\sigma_y^2(0)}\left(y - \frac{\mathrm{L}_y}{2}\right)^2 - \frac{1}{4\sigma_z^2(0)}\left(z - \frac{\mathrm{L}_z}{2}\right)^2\right]$$

$$\sigma_y^2(x) \equiv \sigma_{y0}^2 + \frac{i}{2k_0}\left(x - \frac{\mathrm{L}_x}{2}\right)$$

$$\sigma_z^2(x) \equiv \sigma_{z0}^2 + \frac{i}{2k_0}\left(x - \frac{\mathrm{L}_x}{2}\right),$$

where I_0 is the diffraction-limited intensity of the laser and σ_{y0} and σ_{z0} are the transverse widths of the laser at the focal plane.

Initially ($t = 0$), the plasma is spatially uniform, and the initial condition for $\mathbf{a}$ is

$$\mathbf{a}(x, y, z, 0) = \hat{\mathbf{e}}_z \frac{\sigma_{y0}\sigma_{z0}}{\sigma_y(x)\sigma_z(x)} \left(\frac{8\pi \mathrm{I}_0}{c\omega_0^2}\right)^{1/2} \exp\left[-\frac{1}{4\sigma_y^2(x)}\left(y - \frac{\mathrm{L}_y}{2}\right)^2 - \frac{1}{4\sigma_z^2(x)}\left(z - \frac{\mathrm{L}_z}{2}\right)^2\right],$$

where $\mathrm{K}_0 = \mathrm{K}(x, y, z, 0)$ is simply a constant.

The boundary conditions presented in this section assume that the electromagnetic waves propagate at sufficiently small angles relative to the x direction. Electromagnetic waves propagating at large angles relative to the x direction will suffer artificial reflections at the boundaries. In the regimes of interest to the ICF effort, the lasers typically have an f/number of 2–8, which means that in the absence of plasmas, the largest wave-propagation angle with respect to the x direction is about 14°. An examination of the reflectivity at the boundaries $x = 0, \mathrm{L}_x$ at $t = 0$ as a function of scattering angles (results not shown) shows that the reflectivity is very small and is dominated by Thomson scattering of the initial noise in the plasma density. Hence, artificial reflections at the boundaries are not of concern for situations of interest to the ICF effort.

4. TIMING STUDIES

The code has been tested in three dimensions, and two timing studies have been performed to assess the degree of parallel efficiency of the code. Details of these timing studies are as follows.

Test simulations with a computational mesh of $4096 \times 64 \times 64$ (16 million) cells and 16 ion particles per computational cell (a total of 256 million ion particles) is performed. More details regarding the plasma parameters and laser characteristics for these simulations can be found in Section 5. First, the total CPU time required for the simulations is recorded and is divided by the number of time steps in order to obtain the average CPU time required for each time step. The number of processors, the number of computation cells, and the total number of particles are varied together so that the number of computation cells and the

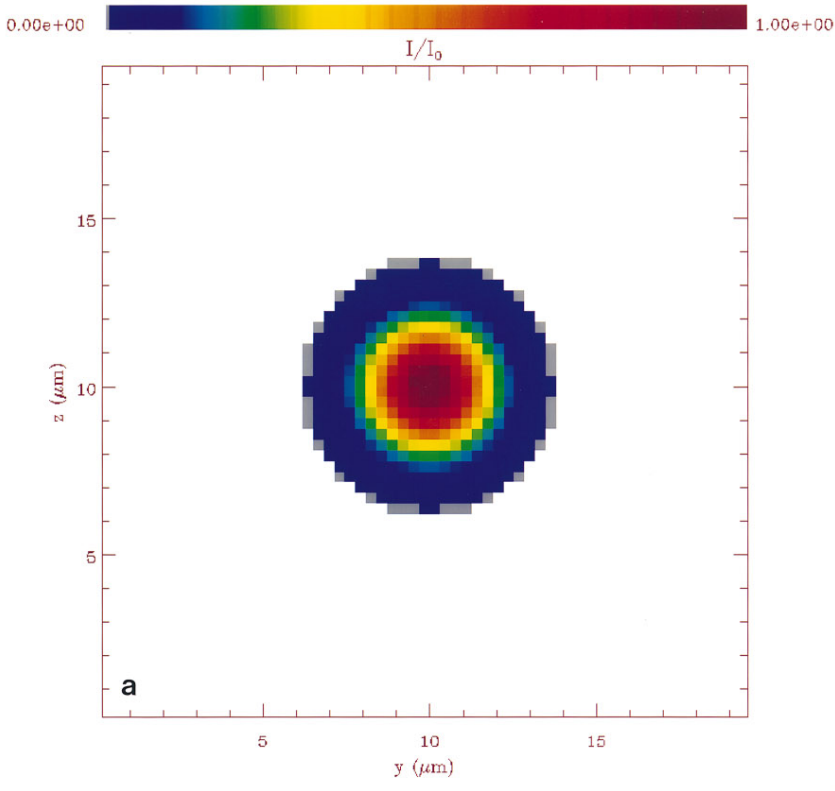
0.00e+00
1.00e+00
I/I0
15
10
5
z (μm)
a
5
10
15
y (μm)

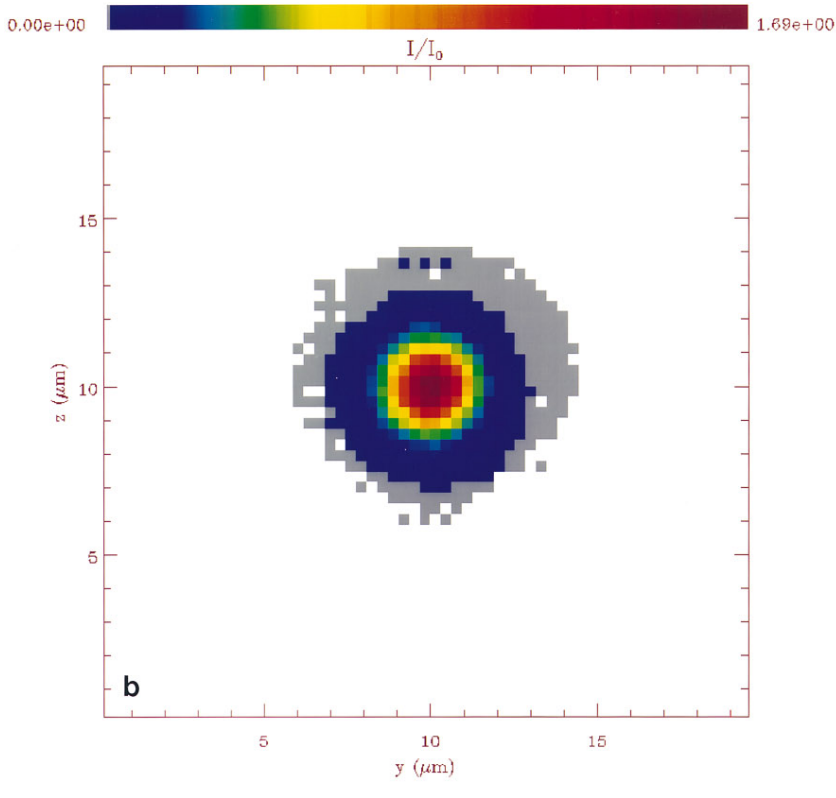
0.00e+00
1.69e+00
I/I0
15
10
5
z (μm)
b
5
10
15
y (μm)

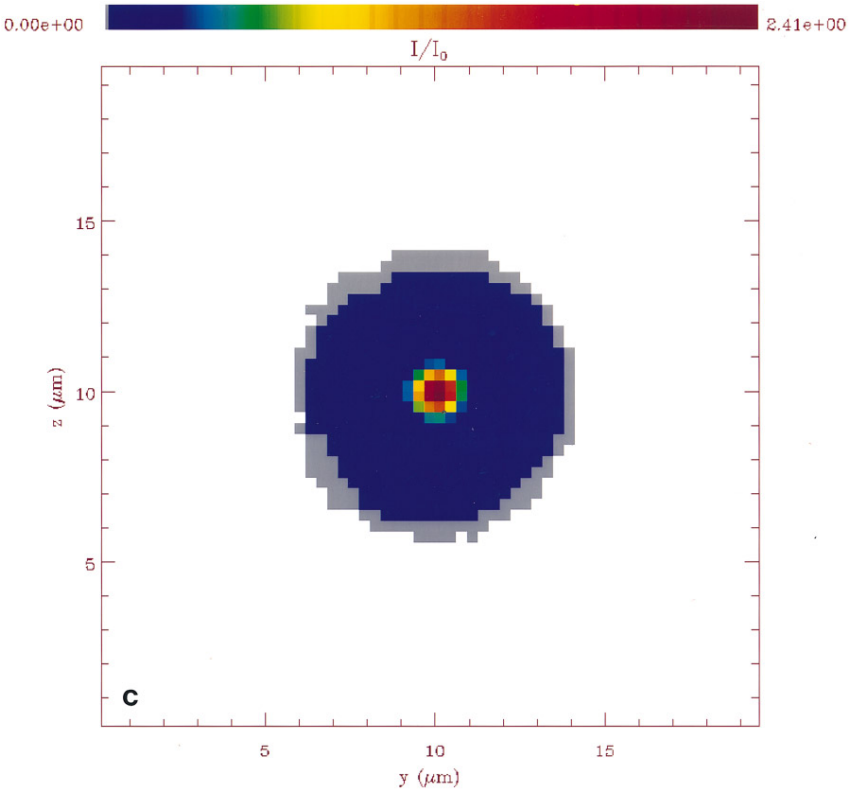

FIG. 2. Color-coded contour plots of the normalized laser intensity (I/I_0) on the laser-exit plane $(x = L_x)$ at three different times: (a) $\Omega_{pH}t = 0$; (b) $\Omega_{pH}t = 40$ (100 ps); and (c) $\Omega_{pH}t = 65$ (160 ps), respectively. The plasma has no transverse motion.

number of particles per processor remain constant. The results are summarized in Table 1. The average CPU time required to execute one time step remains nearly constant, as one would expect. On average, it is found that the amount of CPU time is expended in the following manner: (a) calculating the ion density by interpolating from particle data onto the computational mesh via Eq. (11) requires 46% of CPU time ($\sim$0.24 μs/particle/time step), (b) solving for the scalar and vector potentials from Eqs. (12)–(14) requires 20% of CPU time ($\sim$2 μs/computational cell/time step), and (c) updating particle velocities and positions via Eq. (15) requires 34% of CPU time ($\sim$0.18 μs/particle/time step).

Second, a simulation of fixed size is performed in which the number of processors is varied, and the results are summarized in Table 2. The last column of Table 2 shows the speedup factor compared with the situation in which only half as many processors are

TABLE 1

No. of processors	Grid size	No. of particles/cell	CPU seconds
64	$512 \times 64 \times 64$	16	136
128	$1024 \times 64 \times 64$	16	148
256	$2048 \times 64 \times 64$	16	145
512	$4096 \times 64 \times 64$	16	143

TABLE 2

No. of processors	Grid size	No. of particles/cell	CPU seconds	Speedup
64	$512 \times 64 \times 64$	16	136	
128	$512 \times 64 \times 64$	16	73	1.86
256	$512 \times 64 \times 64$	16	38	1.92
512	$512 \times 64 \times 64$	16	20	1.90

available. For a perfectly scaleable parallel code, one expects the average time required to execute one time step to be halved when the number of processors is doubled. For our code, it can be seen from the last column of Table 2 that the speedup factor is about 1.9 whenever the number of processors is doubled. The results shown in Tables 1 and 2 indicate that our code has a high degree of parallel efficiency.

5. RESULTS AND DISCUSSION

Test simulations with and without plasma flow transverse to the direction of propagation of the pump electromagnetic field are presented.

A. *Self-Focusing without Plasma Flow*

When a coherent laser propagates a plasma, two competing physical mechanisms, which occur simultaneously, affect the propagation of the laser: (1) diffraction defocuses the laser beam, and (2) formation of a plasma channel which focuses the laser beam. For sufficiently low laser intensities, diffraction is the dominant effect, and the laser beam defocuses as it propagates through the plasma. However, for sufficiently high laser intensities, the formation of the self-guiding plasma channel is the dominant effect, and the laser beam focuses as it propagates through the plasma. This is commonly known as self-focusing [34]. It is in this regime of self-focusing that the simulation, to be described below, is performed.

The simulation is performed in a rectangular simulation box with $L_y = L_z = 20\,\mu$m, and $L_x = 50\,\mu$m. The diffraction-limited laser intensity I_0 is taken to be 5×10^{16} W/cm^2. The widths of the laser beam, σ_{y0} and σ_{z0}, are taken to be $L_y/16$ and $L_z/16$, respectively. ω_0, the frequency of the incident laser, is taken to be 5.37×10^{15} Hz and corresponds to a frequency-tripled Nd-Glass laser with vacuum wavelength $\lambda_v = 0.351\,\mu$m. It can be shown that the focal plane of the laser is at $x = L_x/2$, and that the laser has an f/number of 22 (the f/number is defined to be the ratio of the focal length of the optical lens to its diameter). Initially, the plasma is spatially uniform and stationary.

The plasma consists of protons and helium ions with $n_{\rm H} = n_{\rm He} = n_e/3$, $T_e = 5$ keV, and $T_{\rm H} = T_{\rm He} = 0.5$ keV. The electron density is taken to be 8.9×10^{20}cm^{-3}. The ratio of specific heats γ is taken to be 1. The simulation box has $4096 \times 64 \times 64$ (16 million) computational cells, and each ion species is represented by eight particles per computational cell (a total of 256 million ion particles). For this simulation, $\Omega_{p\rm H}\delta t = 0.1$, where $\Omega_{p\rm H}$ is the proton plasma frequency. In principle, SBS, FI, and SF parametric processes can coexist. However, for this particular simulation, only SBS and SF are observed to occur simultaneously. For an example of a simulation in which SBS and FI coexist, see Ref. [33].

Figures 2a, 2b, and 2c are color-coded contour plots of the laser intensity, normalized to the diffraction-limited intensity I_0, $I/I_0 = c\omega_0^2 \mathbf{a} \cdot \mathbf{a}^*/8\pi I_0$ on the laser-exit plane ($x = L_x$)

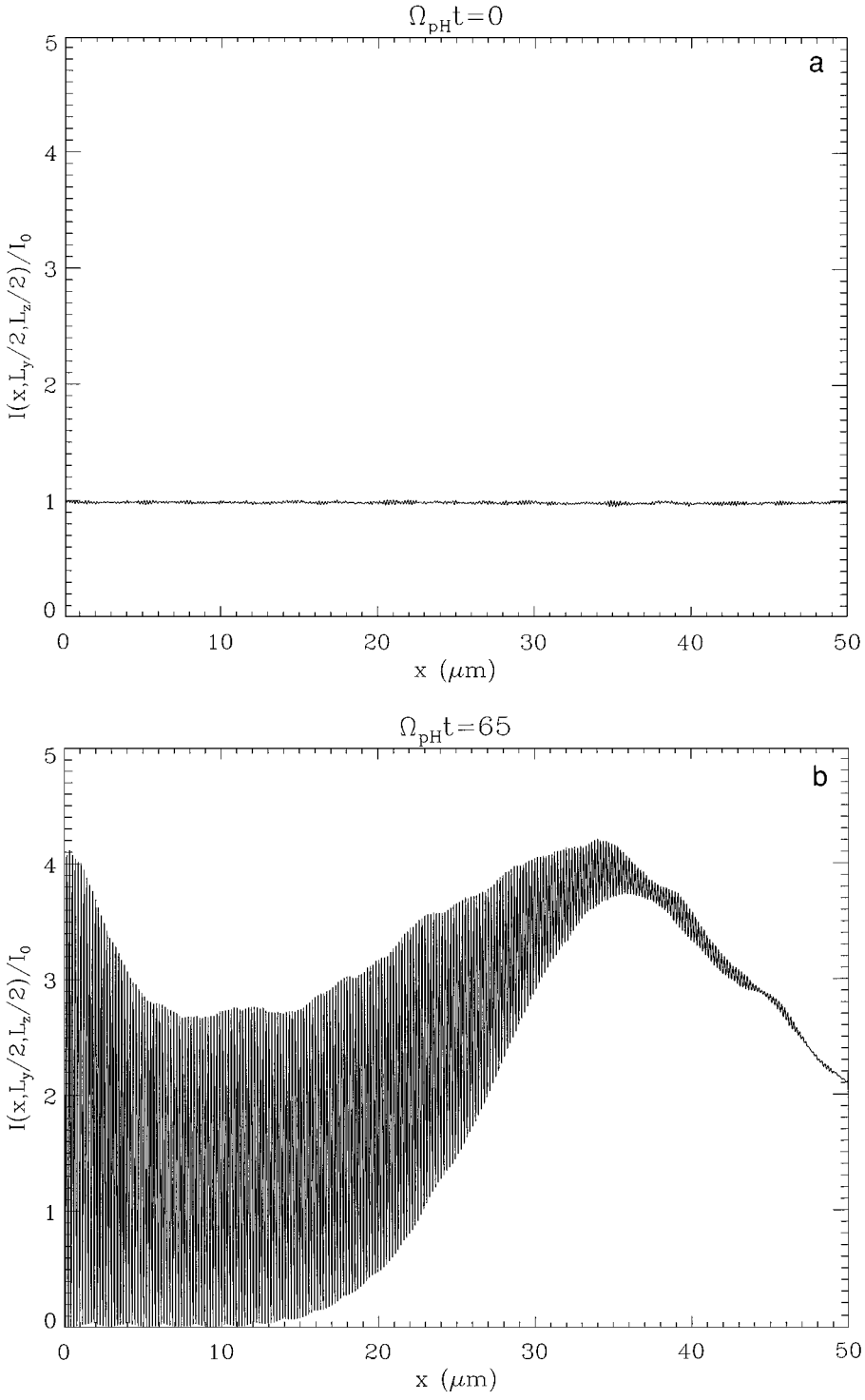

FIG. 3. Normalized laser intensity (I/I_0) along the center of the laser beam ($y = L_y/2, z = L_z/2$) at two different times: (a) $\Omega_{prmH}t = 0$; (b) $\Omega_{pH}t = 65$ (160 ps).

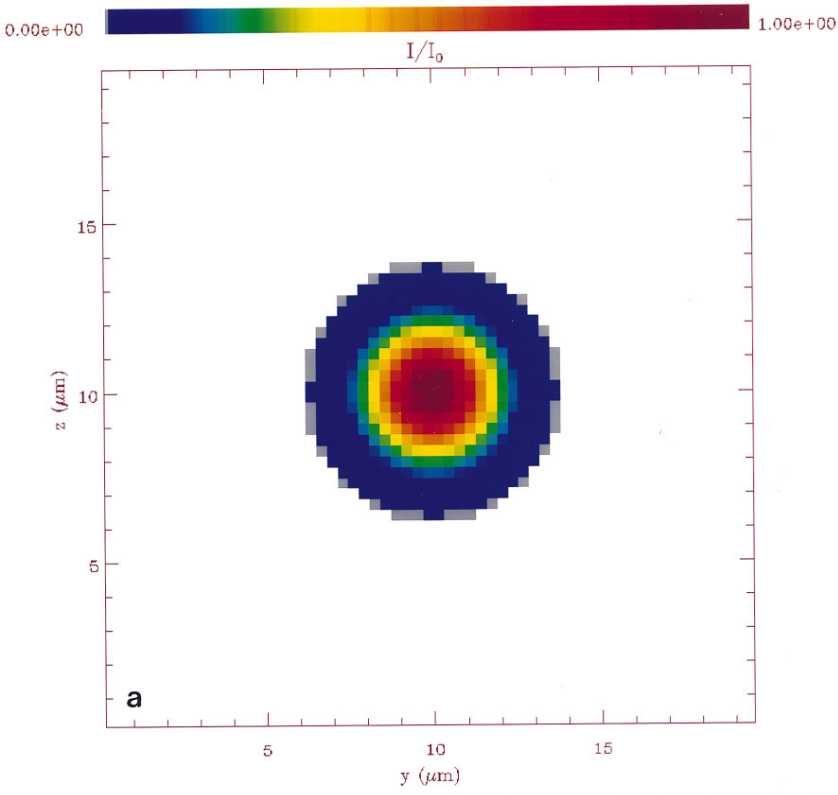
0.00e+00
1.00e+00
I/I0
15
10
5
z (μm)
a
5
10
15
y (μm)

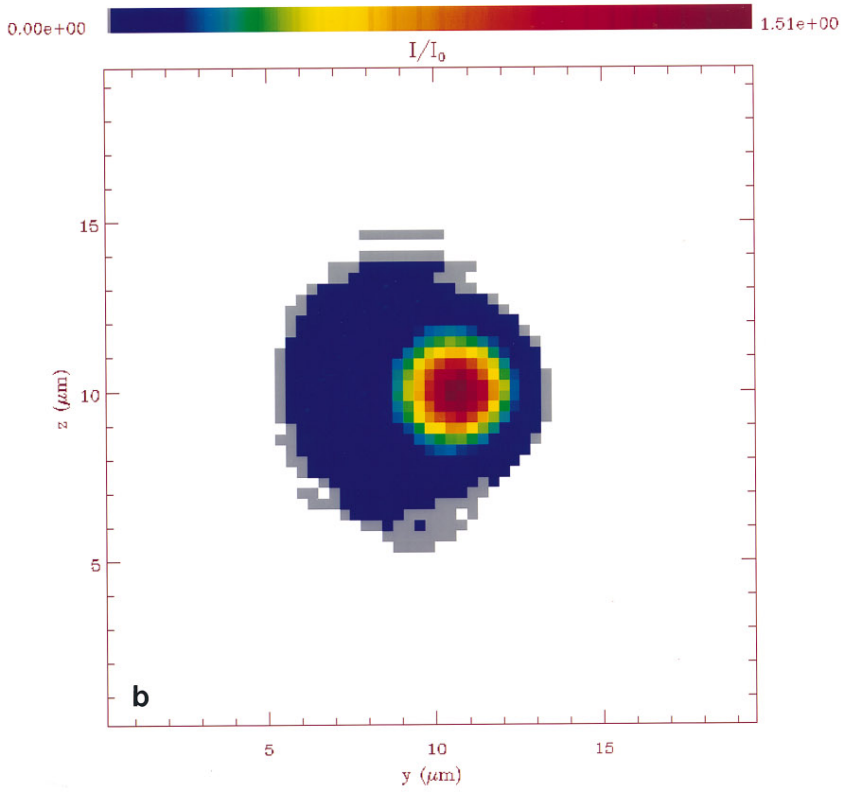
0.00e+00
1.51e+00
I/I0
15
10
5
z (μm)
b
5
10
15
y (μm)

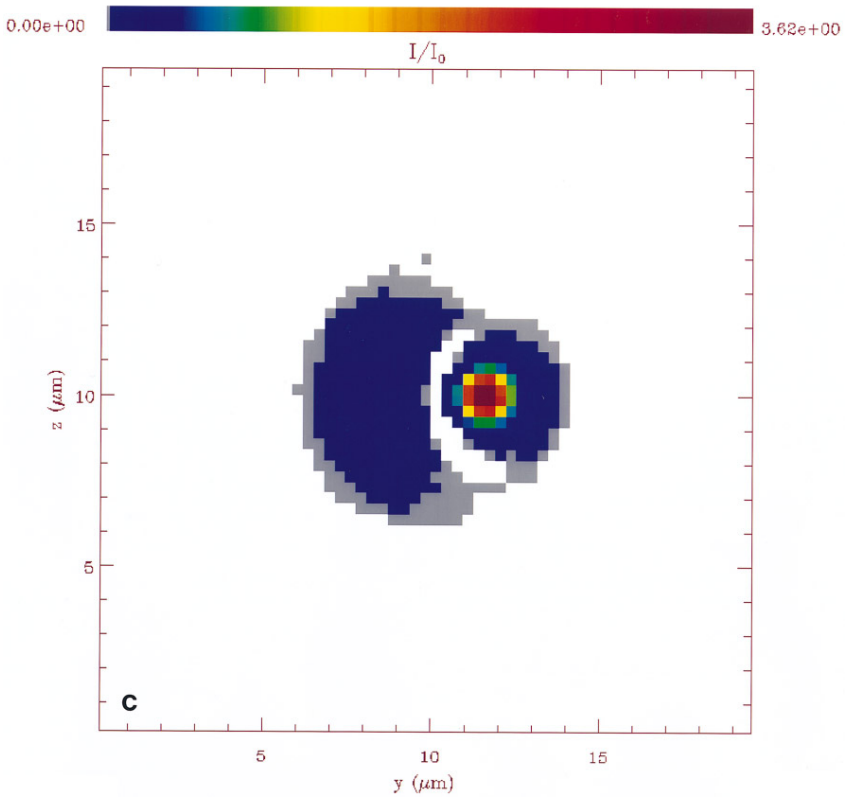

FIG. 4. Color-coded contour plots of the normalized laser intensity (I/I_0) on the laser-exist plane $(x = L_x)$ at three different times: (a) $\Omega_{pH}t = 0$; (b) $\Omega_{prmH}t = 40$ (100 ps); (c) $\Omega_{pH}t = 65$ (160 ps), respectively. The plasma has a sonic flow in the y-direction.

at times $\Omega_{pH}t = 0$, 40, and 65, respectively. Figures 2 indicate that as time progresses, the laser beam self-focuses to a smaller spot.

Figures 3 consist of plots of laser intensity, normalized to I_0, as a function of the axial distance x, at the center of the beam $(y = L_y/2, z = L_z/2)$ for $\Omega_{pH}t = 0$, and 65 (10.5 ps), respectively. The presence of strong SBS at $\Omega_{pH}t = 65$ is evidenced by the short-wavelength spatial modulation in the laser intensity, which is caused by the beating of the incident and backscatter waves. The SBS reflectivity, defined as the ratio of the reflected wave intensity to the incident wave intensity, is nearly 100% at $\Omega_{pH}t = 65$. For reference, it is noted here that for the plasma parameters under consideration, $\Omega_{pH}t = 65$ corresponds to $t = 160$ ps.

An interesting feature of Figs. 2 is that at time $\Omega_{pH}t = 65$ when self-focusing reduces the cross-sectional area of the laser beam by about an order of magnitude, the laser intensity, in fact, does not increase correspondingly by an order of magnitude. This is due to the fact that in the presence of strong SBS, as indicated by Figs. 3, the incident laser intensity is depleted significantly near the laser exit plane. A time-history of the total energy (not shown) indicates that throughout the simulation, the total energy is conserved to within 2%.

It is noted here that for the simulation under consideration, the spatial resolution in the directions perpendicular to the laser propagation direction is $\delta y = \delta z \approx \lambda$. Although this spatial resolution may seem coarse, it will resolve the physics adequately. From physical

considerations, self-focusing does not reduce the transverse dimensions of the laser beyond a laser wavelengthfor the range of laser intensities in which the model presented in this paper is valid. If physical parameters are such that self-focusing is sufficiently strong to reduce the transverse dimensions of the laser beyond a laser wavelength , the model presented here will break down anyway because physical processes not included in the model, e.g., electron kinetic effects and polarization effects, will be important. Hence, within the confines of parameter space in which the model is valid, one does not expect self-focusing to be sufficiently strong that one must require $\delta y \ll \lambda$ and $\delta z \ll \lambda$. As a matter of practically, if one requires that $\delta y = \delta z \ll \lambda$, instead, the time step δt allowed is reduced and has to be determined according to Eq. (A4) in order to ensure numerical convergence of the line–Jacobi algorithm used in solving the nonlinear Schrodinger equation. The combination of smaller time steps, a larger number of computational cells, and a larger number of finite-size particles demand more resources than a CRAY-T3D with 512 processors can provide. One can, however, choose to simulate smaller physical systems than the simulations presented in this paper. However, since no additional physics is expected to be recovered, this approach has not been undertaken.

With $n_e/n_c = 0.1$, $\theta_{\max}$, the largest scattering angle allowed (see Section 3E), is approximately 48°, and the simulation remains accurate when sidescatter electromagnetic waves occur at angles smaller than $\theta_{\max} = 48°$. This is, in fact, the case for the simulation under consideration.

It is also noted here that, since the boundary condition is periodic in the *y* and *z* directions, it may be possible for electromagnetic waves and ion acoustic waves with large angles of propagation (relative to the *x* direction) to be recycled within the simulation domain, giving rise to unphysical results. In order to avoid such situations, the transverse dimensions of the simulation domains have been chosen sufficiently large that no wave-recycling occurs.

B. *Self-Focusing with Plasma Flow*

In the presence of transverse plasma flows and sufficiently strong ion Landau damping, the self-guiding plasma channel (due to the laser beam, as discussed in Section 5A) is displaced in the direction of the transverse plasma flows. Consequently, the laser beam is refracted in the direction of the plasma flows, resulting in a change of laser propagation direction. Here, a simulation is performed in which laser beam bending is observed.

For the simulation described in Section 5A, it can be shown that the ion acoustic speed, normalized to the speed of light, is approximately 2×10^{-3} [33, 35]. A simulation is performed in which the plasma flow is sonic and is initially in the *y* direction (transverse to the laser propagation direction). All other parameters are identical to the simulation described in Section 5A. Figures 4a, 4b, and 4c are color-coded contour plots of the normalized laser intensity on the laser-exit plane at times $\Omega_{pH}t = 0$, 40, and 65, respectively. A comparison of Figs. 2 (without transverse flow) and 4 (with transverse flow) shows that in the presence of a transverse plasma flow, the laser beam is deflected in the direction of the flow by about 1.7°. The deflection of the laser beam by a transverse plasma flow has been observed experimentally [36–37], and although the effect of beam deflection has been analyzed and simulated within the context of fluid models [38–40], the simulation presented in this section is the first fully three-dimensional particle-in-cell study of this effect. For the particular case under consideration, the SBS reflectivity is only about 40%, compared with 100% for the case where the transverse plasma flow is absent. Thus, in addition to

the deflection of the laser beam, the transverse plasma flow tends to weaken SBS. It is noted here that a simple fluid model, which accounts for two transverse dimensions and for nonlinear hydrodynamics, yields a beam deflection angle of about 3° [41]. This is in good agreement with our simulation result, given that the simple fluid model does not account for processes such as SBS and self-focusing that tend to affect the beam deflection angle.

C. *Small f/Number Simulation*

Recent experiments in which a nearly diffraction-limited laser beam interacts with a plasma to produce filamentation, SBS, self-focusing, and energetic ions, have been reported [42]. The physical size of the plasma ($\sim 250\,\mu\text{m} \times 64\,\mu\text{m} \times 64\,\mu\text{m}$) and the duration of the laser pulse (100 ps FWHM) are such that the entire experiment can be simulated with our present three-dimensional hybrid code. Simulations of such experiments using our code, and comparisons with actual experimental data, are ongoing [43]. Here, one such simulation is presented at early times for illustrative purposes.

The plasma consists of protons and carbon ions with $n_{\text{H}} = n_{\text{C}} = n_e/7$, $\text{T}_e = 1\,\text{keV}$, and $\text{T}_{\text{H}} = \text{T}_{\text{C}} = 0.5\,\text{keV}$. The electron density is taken to be $8.9 \times 10^{19}\,\text{cm}^{-3}$. The ratio of specific heats γ is taken to be 1. The simulation box has $4096 \times 64 \times 64$ (16 million) computational cells, and each ion species is represented by eight particles per computational cell (a total of 256 million ion particles). For this simulation, $\Omega_{p\text{H}}\delta t = 0.05$, where $\Omega_{p\text{H}}$ is the proton plasma frequency. The laser has a vacuum wavelength of 1.06 μm and is modeled as a diffraction-limited beam with f/number of 4. The diffraction-limited laser intensity I_0 is $5 \times 10^{15}\,\text{W/cm}^2$.

Figures 5a and 5b are color-coded contour plots of the laser intensity, normalized to the diffraction-limited intensity I_0, on the plane of symmetry defined by $z = 0$, at times $\Omega_{p\text{H}}t = 0$, and 50 (10.5 ps), respectively. Figures 5 indicate that there are significant SBS activities and that the laser beam becomes asymmetric in the laser propagation direction. The laser beam, however, remains symmetric in the transverse directions. The beam, as shown in Figs. 5, tends to disperse wider in the transverse plane. This is in qualitative agreement with the experimental observations [44]. For this particular simulation, the maximum resolvable angle (with respect to the x-direction) is $\theta_{\max} = 48°$. As seen from Figs. 5, the laser beam, at time $\Omega_{p\text{H}}t = 50$, has a cone angle of about 30° (with respect to the x-direction. Consequently, the simulation is still in a regime where there is adequate angular resolution of the scattered waves.

6. SUMMARY AND CONCLUSIONS

In this report, a massively parallel three-dimensional hybrid code, implemented on the CRAY-T3D, appropriate for modeling ion-driven parametric instabilities in laser-driven plasmas is presented. This code is a parallelization and three-dimensional extension of an earlier two-dimensional code [33]. The model consists of a Schrodinger-like equation for the vector potential, a Poisson equation for the scalar potential, an exactly integrable electron momentum equation, and the equations of motion for the finite-size ion particles. The Schrodinger equation is solved by a line–Jacobi iterative algorithm, and the Poisson equation is solved by a standard conjugate gradient algorithm without preconditioning. Both of these algorithms are naturally suitable for the CRAY-T3D. An analysis of the line–

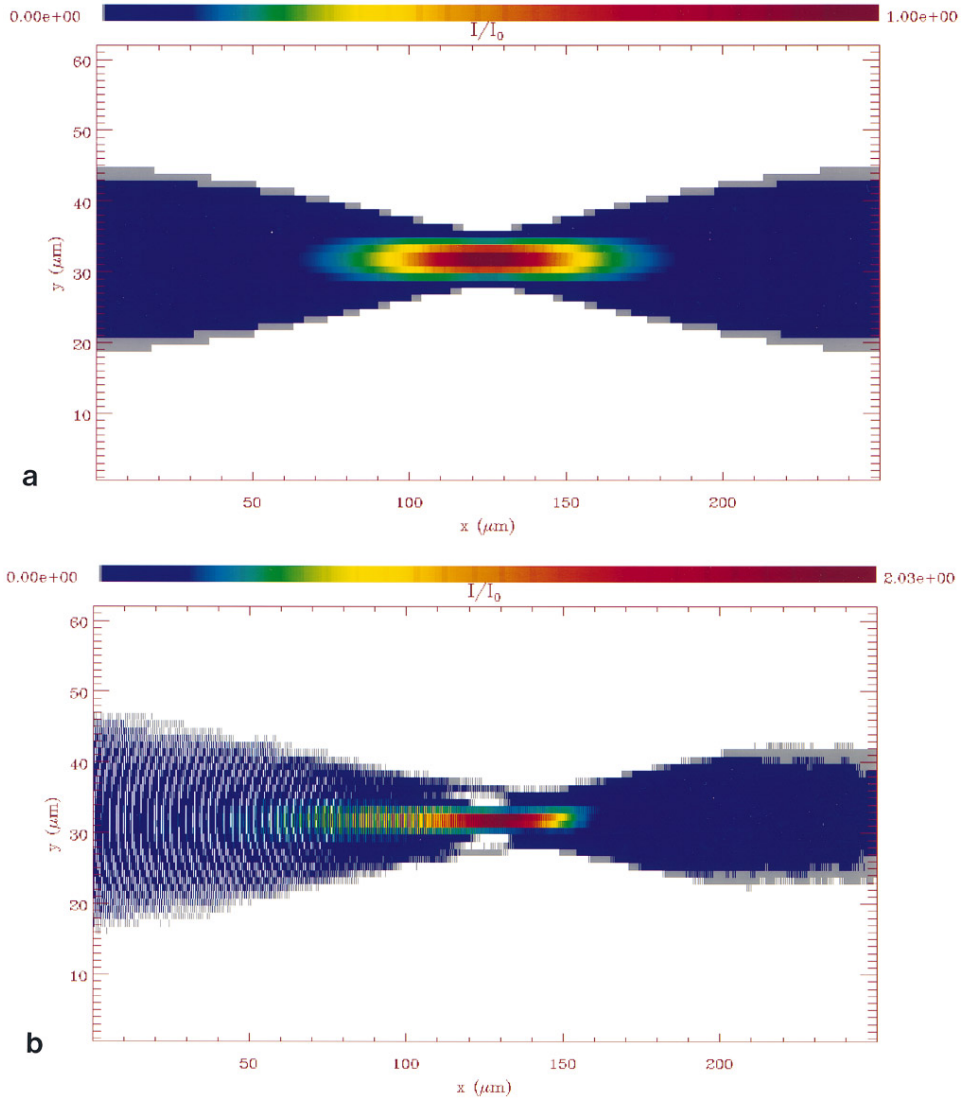

FIG. 5. Color-coded contour plots of the normalized laser intensity (I/I_0) on the plane of symmetry $z = 0$ at two different times: (a) $\Omega_{pH}t = 0$; (b) $\Omega_{pH}t = 50$ (10.5 ps). The plasma has no transverse motion.

Jacobi algorithm is included in the Appendix. It was shown that for typical simulations, the line–Jacobi algorithm is stable for any δt and, therefore, does not place any restriction on the time step.

Three-dimensional simulations of the self-focusing instability with and without plasma flow transverse to the external electromagnetic field have been performed. The results show that in the absence of transverse plasma flow, the cross-section area of the laser beam tends to decrease with the propagation distance into the plasma. This effect is known as self-focusing and results from the self-consistent interaction between the plasma and the laser. In the presence of transverse plasma flows, the results indicate that the laser beam is bent into the direction of the plasma flow. This effect is due to collisionless damping and is qualitatively consistent with previous fluid theory and simulations [4–7].

In our test simulations for which there are 16 particles/cell, it was found that with 512 processors, the code requires about 0.6 μs/particle/time step. The timing results indicate that code has a high degree of efficiency, evidenced by the fact that the CPU time required is reduced by a factor of 1.9 whenever the number of processors is doubled. In test simulations (not shown) with the number of particles per computational cell $\sim O(10^2)$, the code requires only $\sim 0.4\,\mu$s/particle/time step.

Recent experiments suggest that the interaction between electron-driven and ion-driven parametric instabilities may be a credible saturation mechanism for these instabilities [45]. In the near future, we are planning to include electron kinetic effects in HERCULES in order to investigate the interplay between electron-driven and ion-driven instabilities.

APPENDIX: LINE–JACOBI METHOD APPLIED TO SCHRODINGER EQUATION

In general, the line–Jacobi algorithm described in Eq. (17) cannot be analyzed because the matrix coefficients are functions of the indices k, l, and m and are not analytically known functions. In order for the analysis to be more tractable, the electron and ion densities are assumed to be nearly uniform and the external electromagnetic field is taken to be sufficiently weak that density perturbations arising from the interaction between the external field and the plasma is negligible. Under these conditions, $k_0^2 \approx [\mathbf{K}_{\mathrm{NR}}^{(n)}]^2 \approx [\mathbf{K}^{(n-1)}]^2$, and the submatrix C_{lm} can be approximated as follows:

$$\mathbf{C}_{lm}^{k,k} \approx -\left(\frac{1}{\delta x^2}+\frac{1}{\delta y^2}+\frac{1}{\delta z^2}\right)+i\left(\frac{2\omega_0}{c^2\delta t}\right)+\frac{1}{2}k_0^2$$

$$\mathbf{C}_{lm}^{k,k\pm1} = \frac{1}{2\delta x^2}.$$

The eigenvalues λ of the line–Jacobi algorithm can be obtained by solving the equation

$$\lambda \mathrm{C}_{lm}\mathbf{e}_{lm} = -\mathrm{N}_{lm}(\mathbf{e}_{l+1,m}+\mathbf{e}_{l-1,m}) - \mathrm{E}_{lm}(\mathbf{e}_{l,m+1}+\mathbf{e}_{l,m-1}), \tag{A.1}$$

where $\mathbf{e}$ is the eigenvector associated with λ. It can be deduced from Eq. (12) that the eigenvector $\mathbf{e}$ must be of the form:

$$\mathbf{e}_{lm}^{k} = \exp\left(i\frac{kk'\pi}{\mathrm{N}_x}\right)\exp\left(i\frac{ll'\pi}{\mathrm{N}_y}\right)\exp\left(i\frac{mm'\pi}{\mathrm{N}_z}\right). \tag{A.2}$$

Substituting Eq. (A.2) into Eq. (A.1), one obtains

$$\lambda = \left\{\frac{\frac{1}{\delta y^2}\cos\left(\frac{l'\pi}{\mathrm{N}_y}\right)+\frac{1}{\delta z^2}\cos\left(\frac{m'\pi}{\mathrm{N}_z}\right)}{\frac{1}{\delta x^2}+\frac{1}{\delta y^2}+\frac{1}{\delta z^2}-\frac{1}{2}k_0^2-\frac{1}{\delta x^2}\cos\left(\frac{k'\pi}{\mathrm{N}_x}\right)+i\left(\frac{2\omega_0}{c^2\delta t}\right)}\right\}, \tag{A.3}$$

where $1 \le k' \le \mathrm{N}_x - 1$, $1 \le m' \le \mathrm{N}_y - 1$, and $1 \le l' \le \mathrm{N}_z - 1$. The line–Jacobi algorithm converges when the spectral radius (the largest norm of the eigenvalues) is bounded by unity:

$$\max\left\{\frac{\left[\frac{1}{\delta y^2}\cos\left(\frac{\pi}{\mathrm{N}_y}\right)+\frac{1}{\delta z^2}\cos\left(\frac{\pi}{\mathrm{N}_z}\right)\right]^2}{\left[\frac{1}{\delta x^2}+\frac{1}{\delta y^2}+\frac{1}{\delta z^2}-\frac{1}{2}k_0^2 \pm \frac{1}{\delta x^2}\cos\left(\frac{\pi}{\mathrm{N}_x}\right)\right]^2+\left(\frac{2\omega_0}{c^2\delta t}\right)^2}\right\} < 1. \tag{A.4}$$

When conditions are such that Eq. (A.4) is satisfied, the line–Jacobi algorithm will converge at the following asymptotic rate:

$$\mathrm{R} = -\log\left[\max\left\{\frac{\left[\frac{1}{\delta y^2}\cos\left(\frac{\pi}{\mathrm{N}_y}\right)+\frac{1}{\delta z^2}\cos\left(\frac{\pi}{\mathrm{N}_z}\right)\right]^2}{\left[\frac{1}{\delta x^2}+\frac{1}{\delta y^2}+\frac{1}{\delta z^2}-\frac{1}{2}k_0^2\pm\frac{1}{\delta x^2}\cos\left(\frac{\pi}{\mathrm{N}_x}\right)\right]^2+\left(\frac{2\omega_0}{c^2\delta t}\right)^2}\right\}\right]. \tag{A.5}$$

The following interesting property of the line–Jacobi algorithm can be derived from Eq. (A.4). For sufficiently small δx ($k_0\delta x<\sqrt{2}$), the algorithm is convergent for any δt if

$$2\left(\frac{1}{\delta y^2}+\frac{1}{\delta z^2}\right)-\frac{1}{2}\left(\frac{\pi}{L_y}\right)^2-\frac{1}{2}\left(\frac{\pi}{L_z}\right)^2+\frac{1}{2}\left(\frac{\pi}{L_x}\right)^2<\frac{1}{2}k_0^2. \tag{A.6}$$

In most simulations, Eq. (A.6) is satisfied, and the line–Jacobi iterative algorithm places no restriction on the time step. For instance, consider a typical simulation in which $L_x=50\,\mu\mathrm{m}$, $L_y=L_z=11\,\mu\mathrm{m}$, $N_x=4096$, $N_y=N_z=64$, $\omega_0=5.37\times10^{15}\,\mathrm{Hz}$ (frequency-tripled Nd:Glass laser), and $n_e=8.9\times10^{20}\,\mathrm{cm}^{-3}$ (10% of critical density). For these parameters, $k_0=1.7\times10^5\,\mathrm{cm}^{-1}$, $k_0\delta x=0.21<\sqrt{2}$, and Eq. (A.6) is clearly satisfied. With $\omega_0\delta t=60$, the asymptotic rate of convergence is $R=0.38$, and it takes only 10 iterations to reduce the initial error by four orders of magnitude.

ACKNOWLEDGMENT

This work was supported by the Inertial Confinement Fusion Theory and Design Program at Los Alamos. The author thanks Dr. R. J. Kares for many helpful suggestions in programming the CRAY-T3D. The author also thanks Dr. D. Winske.

REFERENCES

1. W. L. Kruer, *The Physics of Laser Plasma Interactions* (Addison–Wesley, New York, 1988).
2. B. J. MacGowan, *Bull. Am. Phys.* **40**, 1645 (1995).
3. J. D. Moody, B. J. MacGowan, R. K. Kirkwood, D. S. Montgomery, R. L. Berger, D. E. Hinkle, T. D. Sheppard, and E. A. Williams, *Bull. Am. Phys.* **40**, 1824 (1995).
4. H. A. Rose, *Phys. Plasmas*, submitted.
5. W. L. Kruer, *Bull. Am. Phys.* **40**, 1824 (1995).
6. D. F. Dubois and H. A. Rose, *Bull. Am. Phys.* **40**, 1824 (1995).
7. E. A. Williams and D. E. Hinkle, *Bull. Am. Phys.* **40**, 1824 (1995).
8. J. M. Dawson, *Rev. Mod. Phys.* **55**, 403 (1983).
9. H. X. Vu and J. U. Brackbill, *Comput. Phys. Commun.* **69**, 253 (1992).
10. J. U. Brackbill and D. W. Forslund, *J. Comput. Phys.* **46**, 271 (1982).
11. D. W. Forslund and J. U. Brackbill, *Phys. Rev. Lett.* **48**, 1614 (1982).
12. J. U. Brackbill and D. W. Forslund, in *Computational Techniques: Multiple Time Scales*, edited by J. U. Brackbill and B. I. Cohen (Academic Press, Orlando, FL, 1985).
13. D. Dickman, R. L. Morse, and C. W. Nielson, *Phys. Fluids* **12**, 1708 (1969).
14. A. B. Langdon, *J. Comput. Phys.* **6**, 247 (1970).
15. A. B. Langdon and B. F. Lasinski, *Methods Comput. Phys.* **16**, 327 (1976).
16. C. W. Nielson and H. R. Lewis, *Methods Comput. Phys.* **16**, 367 (1976).
17. J. Busnardo-Neto, P. L. Pritchett, A. T. Lin, and J. M. Dawson, *J. Comput. Phys.* **23**, 300 (1977).

18. J. A. Byers, B. I. Cohen, W. C. Condit, and J. D. Hanson, *J. Comput. Phys.* **27**, 363 (1978).
19. D. W. Hewett and C. W. Nielson, *J. Comput. Phys.* **29**, 219 (1978).
20. D. W. Hewett, *J. Comput. Phys.* **38**, 378 (1980).
21. R. J. Mason, *J. Comput. Phys.* **41**, 233 (1981).
22. J. Denavit, *J. Comput. Phys.* **42**, 337 (1981).
23. R. J. Mason, in *Computational Techniques: Multiple Time Scales*, edited by J. U. Brackbill and B. I. Cohen (Academic Press, Orlando, FL, 1985).
24. B. I. Cohen, in *Computational Techniques: Multiple Time Scales*, edited by J. U. Brackbill and B. I. Cohen (Academic Press, Orlando, FL, 1985).
25. A. B. Langdon and D. C. Barnes, in *Computational Techniques: Multiple Time Scales*, edited by J. U. Brackbill and B. I. Cohen (Academic Press, Orlando, FL, 1985).
26. R. W. Hockney and J. W. Eastwood, *Computer Simulation Using Particles* (Hilger, New York, 1988).
27. H. X. Vu, J. U. Brackbill, and D. Winske, *J. Geophys. Res.* **97**, 13839 (1992).
28. J. U. Brackbill and H. X. Vu, *Geophys. Res. Lett.* **20**, 2015 (1993).
29. D. W. Forslund, J. M. Kindel, and E. L. Lindman, *Phys. Fluids* **18**, 1017 (1975).
30. A. Ghizzo, T. Reveille, P. Bertrand, T. W. Johnston, J. Lebas, and M. Shouchri, *J. Comput. Phys.* **118**, 356 (1995).
31. K. Estabrook, S. C. Wilks, W. L. Kruer, J. Denavit, D. E. Hinkle, D. Kalantar, A. B. Langdon, B. J. MacGowan, D. Montgomery, J. Moody, and E. A. Williams, *Bull. Am. Phys.* **39**, 1733 (1994).
32. S. C. Wilks, W. L. Kruer, R. L. Berger, E. A. Williams, and J. Denavit, "Studies of Stimulated Brillouin Scattering Using a Hybrid Particle Ion/Fluid Electron Code," in *Proceedings, Twenty Second Annual Anomalous Absorption Conference, Lake Placid, NY, July 1992.*
33. H. X. Vu, *J. Comput. Phys.* **124**, 417 (1996).
34. D. C. Brown, *High-Peak-Power Nd:Glass Laser Systems* (Springer-Verlag, New York, 1981).
35. H. X. Vu, J. M. Wallace, and B. Bezzerides, *Phys. Plasmas* **1**, 3542 (1994).
36. J. D. Moody, B. J. MacGowan, D. E. Hinkle, W. L. Kruer, E. A. Williams, K. Estabrook, T. D. Shepard, R. K. Kirkwood, D. S. Montgomery, and R. L. Berger, *Phys. Rev. Lett.*, submitted.
37. B. S. Bauer and J. C. Fernandez, private communication.
38. H. A. Rose, *Phys. Plasmas* **3**, 1709 (1996).
39. D. E. Hinkle, E. A. Williams, and C. H. Still, *Phys. Rev. Lett.*, submitted.
40. W. L. Kruer, *Bull. Am. Phys.* **40**, 1824 (1995).
41. B. Bezzerides, private communication.
42. P. E. Young, *Phys. Plasmas* **2**, 2815 (1995).
43. In collaboration with P. E. Young and W. L. Kruer of Lawrence Livermore National Laboratory.
44. P. E. Young, private communication.
45. J. C. Fernandez, J. A. Cobble, B. H. Failor, D. F. Dubois, D. S. Montgomery, H. A. Rose, H. X. Vu, B. H. Wilde, M. D. Wilke, and R. E. Chrien, *Phys. Rev. Lett.*, submitted.